AIMS Materials Science, 13(4): 651–670.
DOI: 10.3934/matersci.2026032
Received: 06 June 2026
Revised: 07 July 2026
Accepted: 09 July 2026
Published: 22 July 2026

https://www.aimspress.com/journal/Materials

Research article

The influence of minor Zn and Cu additions on the superplastic deformation behavior and deformation mechanisms of Al-Mg-Mn-Cr-Zr alloy

Zarnigor S. Turaeva[1], Olga A. Yakovtseva[1], Natalia Yu. Tabachkova[1,2], Eugene S. Statnik[1,3], Vladimir V. Cheverikin[1,4] and Anastasia V. Mikhaylovskaya[1,*]

[1] National University of Science and Technology MISIS, Leninsky Prospekt, 4, 119049 Moscow, Russia
[2] Prokhorov General Physics Institute of the Russian Academy of Sciences, Vavilov str. 38, 119991 Moscow, Russia
[3] Skolkovo Institute of Science and Technologies (Skoltech), Bolshoy Boulevard, 30, bld. 1, Moscow 121205, Russia
[4] Moscow State University, 1 Leninskiye Gory, Moscow 119991, Russia

* **Correspondence:** Email: mihaylovskaya@misis.ru.

Abstract: Superplastic forming is an important processing technique for complex shape parts, and the non-heat-treatable Al-Mg-based alloys of 5xxx-series are the most attractive for aerospace and automotive applications. In this work, we investigated the influence of minor additions of Zn and Cu (>1 wt.%) on the superplastic deformation behavior of an Al-5.2Mg-0.9Mn-0.12Cr-0.1Zr alloy over the temperature range of 480–520 °C and constant strain rate range of 10^{-3} to 10^{-2} s^{-1}. The microstructural evolution and contributions of grain boundary sliding (GBS), dislocation slip/creep, and diffusional creep to the total strain were analyzed using scanning electron microscopy and marker grid technique at the steady-state stage of superplastic flow in alloys with a similar mean grain size of about 5.5 μm. The results demonstrated that the addition of Zn increases the GBS contribution from ~30% to ~40%, which improves superplastic performance. In contrast, the Cu addition insignificantly influences GBS but facilitates intragranular deformation and increases cavitation, which weakens superplasticity. The effect of the solute elements is discussed in terms of the influence of their segregation on Al diffusion and the barrier to GBS.

Keywords: aluminum alloy; superplasticity; grain boundary sliding; diffusion creep; dislocation slip/creep; surface structure evolution

1. Introduction

Aluminum-magnesium (Al-Mg) based alloys of the 5xxx series remain essential materials for marine, automotive, and aerospace applications due to their favorable combination of strength, high corrosion resistance, and good weldability [1,2]. Developments in lightweight structural applications demand continuous improvement in the high-temperature formability of these alloys, particularly for superplastic forming operations that enable the production of complex-shaped components [3–6].

Grain size is a key parameter for superplastic behavior, as it controls the transition to grain boundary sliding (GBS). A fine-grained microstructure generally increases the strain-rate sensitivity and promotes superplastic flow at lower temperatures and higher strain rates [7–10]. The high-temperature deformation behavior of fine-grained aluminum alloys is governed by competing mechanisms: grain boundary sliding, dislocation, and diffusion creep [11,12].

High strain-rate sensitivity promotes uniform deformation by inhibiting localized necking, which is a prerequisite for achieving large elongations in superplastic forming [13]. The strain-rate sensitivity exponent (m) is therefore a parameter for identifying the dominant deformation mechanism and assessing the potential for superplastic behavior. Grain boundary sliding is associated with m values above 0.3 for fine-grained alloys, and above 0.5 for severely deformed ultrafine-grained materials [14]. Dislocation creep, characterized by $m \approx 0.2$, dominates at higher strain rates or lower temperatures, while diffusion creep becomes significant at very high temperatures and provides $m \approx 1$ [15,16]. The transition between these mechanisms depends on temperature, strain rate, and grain size, and can be visualized through deformation mechanism maps [17,18].

Direct experimental evidence for GBS using surface marker techniques provides the most reliable means to quantify its contribution to total deformation [15,17,19–21]. This method, which involves depositing fine grids on sample surfaces and measuring boundary offsets after deformation, enables unambiguous identification of GBS as a dominant mechanism. Experimental studies on nanostructured Al-Zn-Mg-Cu alloys processed by high-pressure torsion have demonstrated that GBS can be realized even at relatively low temperatures (170 °C) [22]. This finding underscores the importance of understanding GBS contributions across temperature regimes and alloy compositions.

Microalloying by dispersoid-forming elements is important for superplastic Al-based alloys. The transition elements such as Mn, Cr, and Zr promote the formation of fine precipitates (dispersoids) of the Al_6Mn, ε-$Al_{18}Mg_2Cr_3$, and Al_3Zr phases that effectively pin grain boundaries and dislocations, thereby controlling recrystallization and grain growth during thermomechanical processing due to the Zener pinning mechanism [23–27]. These dispersoids are crucial for maintaining fine-grained structures at elevated temperatures, which is a prerequisite for achieving high strain-rate sensitivity and superplasticity [28–30]. Moreover, dispersoids pinning grain boundaries can influence the deformation behavior and inhibit GBS, as is found in AA5083; the alloy with precipitates of ~45–50 nm exhibits from 10% to 25% of GBS contribution [15,19,31]. Nevertheless, for the fine-grained AA7475 alloy with similar grain and dispersoid sizes, GBS provides above 50% [32]. A similarly high contribution is observed for the 7xxx series alloys with coherent Al_3Zr precipitates

of 10 nm in size [33]. According to [34], the minor Zn addition to the AA5083 alloy with a grain size of about 10 μm facilitates GBS. It is reasonable to suggest that the differences in the GBS contributions depend not only on precipitate parameters but also on solute contents.

The role of Zn in Al-Mg alloys deserves special attention. It has been established that Zn atoms, like Mg atoms, tend to segregate at grain boundaries, forming solute-rich layers that modify boundary properties [22,35,36]. Ab initio modeling by Kuznetsov et al. demonstrated that the formation of a thick segregation layer of Zn at grain boundaries in aluminum is energetically preferable, and this segregation substantially decreases the barriers for grain boundary sliding while affecting the cohesive properties of the boundaries [37]. Based on the same approach, Mg and Cu increase the barriers for GBS [38–41]. The researchers in [15,42] agreed to the theory of a low GBS contribution in Al-Cu-based alloys. The role of copper as a soluble element in Al-Mg alloys has not been established experimentally. However, the element can also be used to improve superplasticity performance in the Al-Mg-Mn alloy, as observed in [43]. The authors explained the better superplastic properties by a reduction in the size of T-phase dispersoids and an increase in the stability of the grain structure.

This fundamental understanding of Zn and Cu segregation behavior provides a basis for explaining the enhanced superplastic characteristics of Zn-modified [34] and Cu-modified [44] Al-Mg alloys. The addition of Zn to high-Mg aluminum-based alloys has a positive influence on corrosion resistance by promoting the spheroidization of grain boundary precipitates and reducing sensitization to intergranular corrosion [45]. This combination of beneficial effects makes Zn a particularly attractive alloying addition for 5xxx series alloys intended for superplastic forming applications in marine environments.

Despite extensive research on superplastic Al-Mg alloys, the specific roles of Zn and Cu additions in the activation of deformation mechanisms in complexly-alloyed Al-Mg based alloys containing dispersoids-forming elements Mn, Cr, and Zr remain insufficiently studied. In this work, we address this gap by investigating the deformation behavior of an Al-5.2Mg-0.9Mn-0.12Cr-0.1Zr alloy with controlled additions of below 1% of soluble Zn and Cu.

We focus on characterizing the effect of the minor Zn and Cu additions on grain size, its temperature and deformation stability, superplastic deformation behavior, and the contributions of the superplastic deformation mechanisms. The contributions of GBS, dislocation slip/creep, and diffusional creep are identified by combining strain-induced microstructural evolution with quantitative analysis of focus ion beam marker grid displacements. By correlating mechanical response with direct evidence of grain boundary sliding, this work establishes the role of Zn and Cu additions in promoting or suppressing specific deformation mechanisms, providing a scientific basis for further optimizing the superplastic forming characteristics of Al-Mg based alloys.

2. Materials and methods

The nominal and actual chemical compositions of the alloys studied are presented in Table 1. The reference alloy of Al-5.2%Mg-0.9%Mn-0.12%Cr-0.1%Zr (wt.%) and the alloys with similar contents of the major elements and minor additions of Zn and Cu were compared. The deviation for 3 points of the spectral analysis was below 0.01 wt.%. The elemental contents were selected based on a similar atomic ratio for the Zn and Cu additions (approximately 0.3 at.% for both alloys at 0.7 wt.% of each element, although a slightly different content was measured in the actual alloys by chemical analysis). A critical consideration was the solubility of these elements in the solid solution at the superplastic

deformation temperatures. The Zn content varied from 0.4 to 0.7 wt.% to determine its effect on superplastic behavior. This range was similar to that of the AA5059 alloy (ASTM standard) and helps to further optimize the alloy composition. The Cu addition was chosen based on data from [43], which demonsrated an improvement in the superplasticity of the 5083-type alloy with Cu addition.

The studied alloys were processed using 99.99 wt.% Al, 99.95 wt.% Mg, 99.95 wt.% Zn, and master alloys of Al-10 wt.% Mn, Al-10 wt.% Cr, Al-53.5 wt.% Cu, and Al-5 wt.% Zr. The total residual iron and silicon content was below 0.1 wt.%. The alloy was prepared in a Nabertherm S3 furnace using a graphite-chamotte crucible. The casting temperature was maintained at 760 ± 20 °C. Ingots with dimensions of 120 × 40 × 20 mm^3 were obtained by casting into a water-cooled copper mold with a cooling rate of approximately 15 K/s.

To homogenize the as-cast microstructure, the ingots were annealed in two stages: first at 350 ± 5 °C for 32 h, followed by 480 ± 5 °C for 6 h. The two-step homogenization annealing resulted in dissolution of the non-equilibrium β-Al_3Mg_2 phase, elimination of Mg dendrite segregation, and the precipitation of Mn-rich Al_6Mn, T-$Al_{20}Mn_3Cu_2$ (for Cu-bearing alloy), and Al_3Zr dispersoids.

The homogenized ingots with an initial thickness of 20 mm were subjected to hot rolling at a temperature of 420 ± 10 °C with a total reduction of 50% to a thickness of 10 mm. The reduction per pass was 0.5–1.0 mm. Cold rolling was performed from 10 to 1 mm (total reduction of 90%) with an intermediate heterogenization annealing at $0.6T_{solvus}$ (solvus temperature) for 32 h to precipitate the β-Al_3Mg_2 phase, providing a particle-stimulated nucleation (PSN) effect [46].

The solidus temperature (incipient melting point, $T_{i.m.}$) was determined for the rolled alloys by differential thermal analysis (DTA) by heating over the temperature range of 400 to 700 °C with a heating rate of 5 K/min using a SETARAM Labsys DSC 1600 calorimeter (data presented in Table 1).

Table 1. Chemical compositions of the investigated alloys (nominal/chemical spectral analysis values) (wt.%).

Alloy	Mg	Mn	Cr	Zr	Zn	Cu	Si	Fe	Al	$T_{i.m.}$, °C
AlMg	5.2/5.2	0.9/0.86	0.12/0.11	0.1/0.10	–	–	0.02	0.06	Bal.	560
AlMg0.4Zn	5.2/5.1	0.9/0.85	0.12/0.13	0.1/0.10	0.4/0.39	–	0.05	0.05	Bal.	557
AlMg0.7Zn	5.2/5.3	0.9/0.85	0.12/0.12	0.1/0.10	0.7/0.70	–	0.04	0.04	Bal.	556
AlMg0.7Cu	5.2/5.1	0.9/0.86	0.12/0.13	0.1/0.11	–	0.7/0.57	0.01	0.04	Bal.	550

The microstructures of as-cast samples, after homogenization and recrystallization annealing, and after superplastic deformation were studied with an optical microscope (Carl Zeiss) and a scanning electron microscope (SEM) TESCAN VEGA 3 LMH. SEM was equipped with an X-MAX 80 energy-dispersive X-ray spectrometer (EDS), and an electron backscattering diffraction (EBSD) EBSD-HKL-NordlysMax detector. The EBSD analysis was conducted using the AZTEC software. Electron images were captured over a selected area of 150 × 150 μm^2 with a step size of 0.3 μm. The grain boundary was classified as a low-angle grain boundary (LAGBs, white-colored in maps) for misorientation angles 2–14° and as a high-angle grain boundary (HAGB, black-colored in maps) for misorientation angles of ≥15°. The fine precipitates were examined using a transmission electron microscope (TEM) JEOL JEM-2000EX equipped with an EDS detector.

Specimens were prepared through mechanical grinding on SiC papers and polishing with a colloidal silica-based suspension using Struers LaboPol-5. To characterize the grain structure, anodic

oxidation in an aqueous solution of HBF_4 was applied, and observations were conducted under polarized light. Thin foils were prepared for TEM study using a Struers TenuPol-5 machine in a 30% HNO_3 methanol solution at a voltage of 23 V and a temperature of minus 24 ± 2 °C.

The liner mean grain size was measured in longitudinal and across directions relative to the strain axis by the random secant method. The volume fraction of precipitates was determined by measuring the proportion of the area they occupied on the sample surface. The number of measurements collected ranged from 300 to 500.

Superplastic behavior was studied using uniaxial tensile tests on a Walter Bai LFM-100 testing machine with a Dion-Pro service pack. Samples with a gauge section of 6 × 14 mm^2 and thickness of 1.0 mm were cut parallel to the rolling direction. The samples were held at the deformation temperature for ~15 min prior to straining. To determine the strain rate *m*, tests with a step-by-step increase in strain rate by a factor of 1.5 were performed. Constant strain-rate tests were conducted within a range of 10^{-3} to 10^{-2} s^{-1} at temperatures of 480–520 °C. The microstructure evolution and deformation mechanisms were studied at a temperature of 480 °C and a constant strain rate of 5×10^{-3} s^{-1}.

To calculate the contributions of grain boundary sliding and intragranular deformation mechanisms, the samples were pre-deformed to a strain of 0.69 and then polished. The grids were milled on the surface of the gauge section using a TESCAN Amber GMU microscope equipped with a focused ion beam (FIB) column. The grid size was 100 × 100 μm^2 with a step size of 2.5 μm, selected based on the average grain size. The samples with markers were subjected to step-by-step further straining with increments of strain e = 0.1–0.15, and the evolution of the surface microstructure was studied using SEM in a secondary electron regime. The contributions of deformation mechanisms to the total strain were calculated using the methodology outlined in [47].

3. Results

In the as-cast state, all alloys exhibit a typical dendritic structure with second phase particles located in the interdendritic spaces, including dark-gray Mg-rich and bright Mn- and Cu-rich phases (Figure 1a–d). The AlMg alloy and Zn-modified alloys (AlMg0.4Zn, AlMg0.7Zn) show a similar morphology of secondary phases (Figure 1a,b). The AlMg0.7Cu alloy exhibits a slightly different distribution of intermetallic particles and the formation of Cu-containing phases (Figure 1c,d). According to the ThermoCalc calculation (database TCAL4) and elemental distribution data, the precipitates of the β-Al_3Mg_2 and Al_6Mn phases are formed in the AlMg and Zn-modified alloys, while T-$Al_{20}Cu_2Mn_3$ and S-Al_2CuMg precipitates are formed in the Cu-modified alloy.

After the two-stage homogenization treatment, the dendritic segregations of Mg, Cu, and Zn are eliminated, and the soluble S- and β- phases are dissolved (Figure 1e–i). Magnesium and zinc are uniformly distributed in the Al matrix, while manganese is localized in insoluble phases (Figure 1h,i). Based on their chemical composition, morphology, ThermoCalc calculation these coarse precipitates are identified as the Al_6Mn phase with dissolved Fe and Cr for the Cu-free alloys. The $Al_{20}Cu_2Mn_3$ (T-phase) is suggested for the Cu-modified alloy. The volume fraction of residual coarse second-phase particles after homogenization range from 0.8 ± 0.2% to 1.1 ± 0.2%.

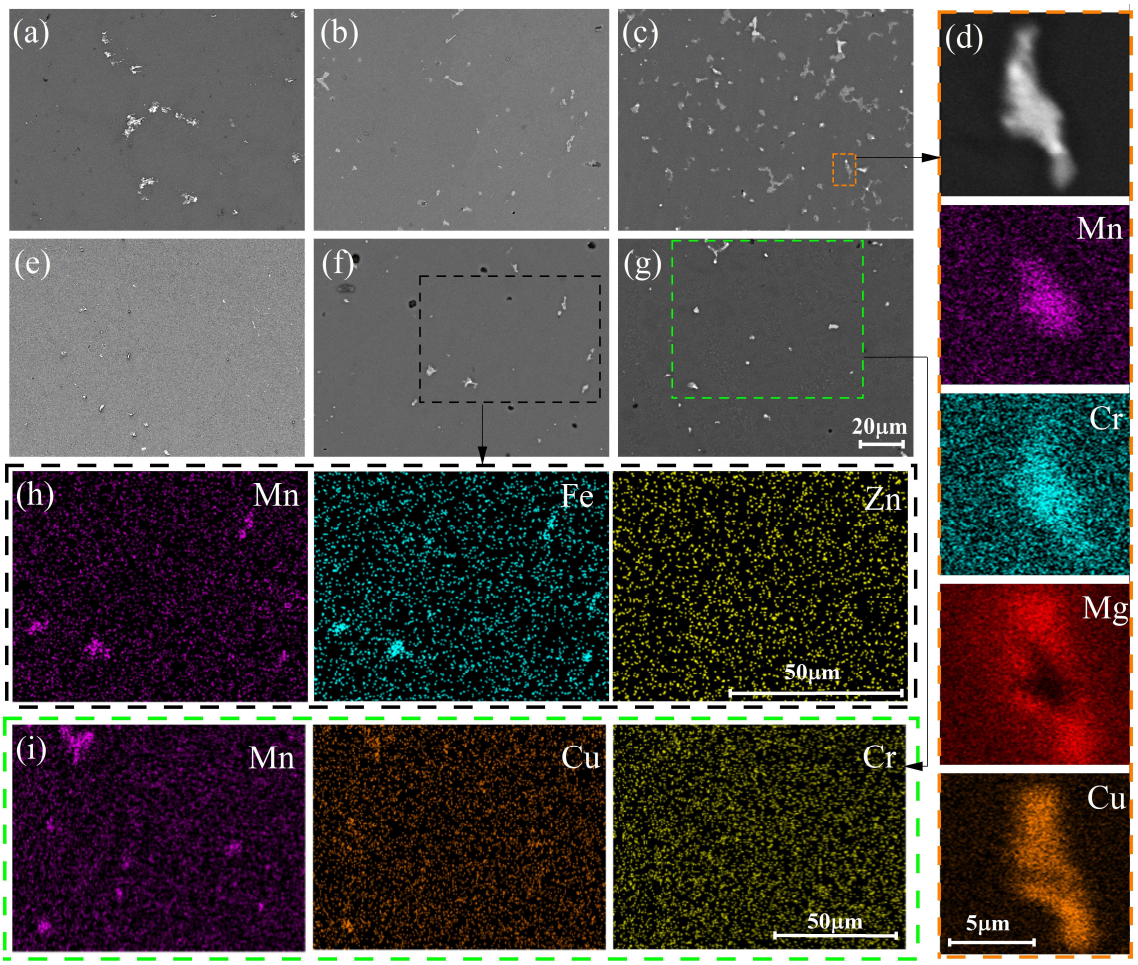

Figure 1. SEM micrographs and EDS maps of (a, e) AlMg, (b, f, h) AlMg0.7Zn, and (c, g, i) AlMg0.7Cu alloys: (a–c) as-cast; (e–g) after homogenization; (d, h, i) EDS maps.

At higher SEM magnifications, fine equiaxed and elongated platelet-like precipitates of the secondary phases (dispersoids), with a total volume fraction of approximately 2%–3%, are observed in as-homogenized state (white colored in Figure 2).

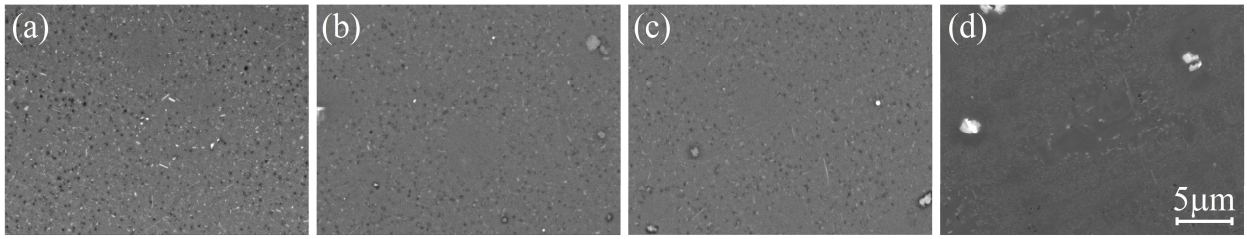

Figure 2. SEM micrographs of alloys after homogenization annealing showing secondary phase dispersoids: (a) AlMg, (b) AlMg0.4Zn, (c) AlMg0.7Zn, and (d) AlMg0.7Cu alloys.

TEM and TEM-EDS studies of the recrystallized alloys confirm the formation of Mn-enriched dispersoids for the Cu-free alloys (Figure 3a–h) and Mn- and Cu-enriched dispersoids for the Cu-bearing alloy (Figure 3i–l). The mean size of the fine Mn-bearing precipitates is (64–71) ± 9 nm. The length

of coarse platelet-like particles varies from 300 to 900 nm for the Cu-free alloys. Coarser platelet-like particles with lengths up to 3 μm are observed in the alloy with Cu. The chemical composition of the equiaxed and elongated precipitates is similar. Depending on the precipitate size and the partial signal from the Al matrix, they contain 3–16 at.% Mn and 0.5–2 at.% Cr in the Cu-free alloys, and 4–16 at.% Mn and 3–11 at.% Cu in the Cu-bearing alloy. Nevertheless, although coarse precipitates form at grain boundaries after annealing, the presence of Cu increases the dispersoid fraction and promotes a uniform distribution across the grain interiors. The dispersoids predominantly belong to the $Al_6(Mn,Cr)$ phase in the Cu-free alloys (Figure 3d). Several precipitates with higher Mn can belong to $Al_4(Mn,Cr)$ phase according to TEM-EDS data (Figure 3h). The $Al_{20}Cu_2Mn_3$ phase is formed in the Cu-bearing alloy (Figure 3l). Finer near-spherical precipitates of the Al_3Zr phase, with a size of about 10 to 20 nm, are observed in all alloys (Figure 3k).

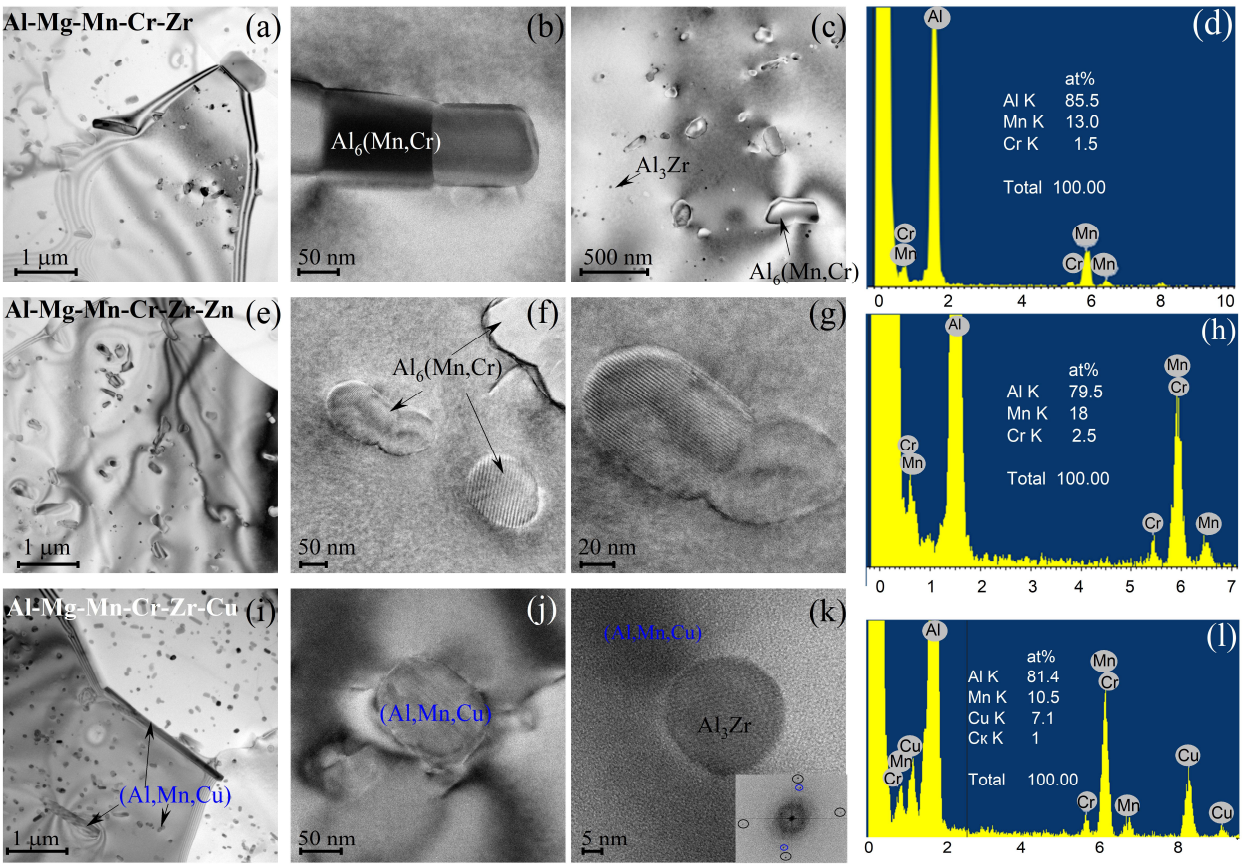

Figure 3. (a–c, e–g, i–k) TEM images and (d, h, l) TEM-EDS spectra from the precipitate areas after annealing of the cold-worked sheet for 20 min at 480 °C in the (a–d) AlMg reference alloy, (e–h) AlMg0.7Zn alloy, and (i–l) AlMg0.7Cu alloy; (f, g, j, k) high resolution images.

Recrystallization leads to the formation of a homogeneous equiaxed fine-grained structure (Figure 4). The grain size differs depending on whether annealing was performed in air with or without preheating in a saltpeter bath (480 °C, 5 min) (Table 2).

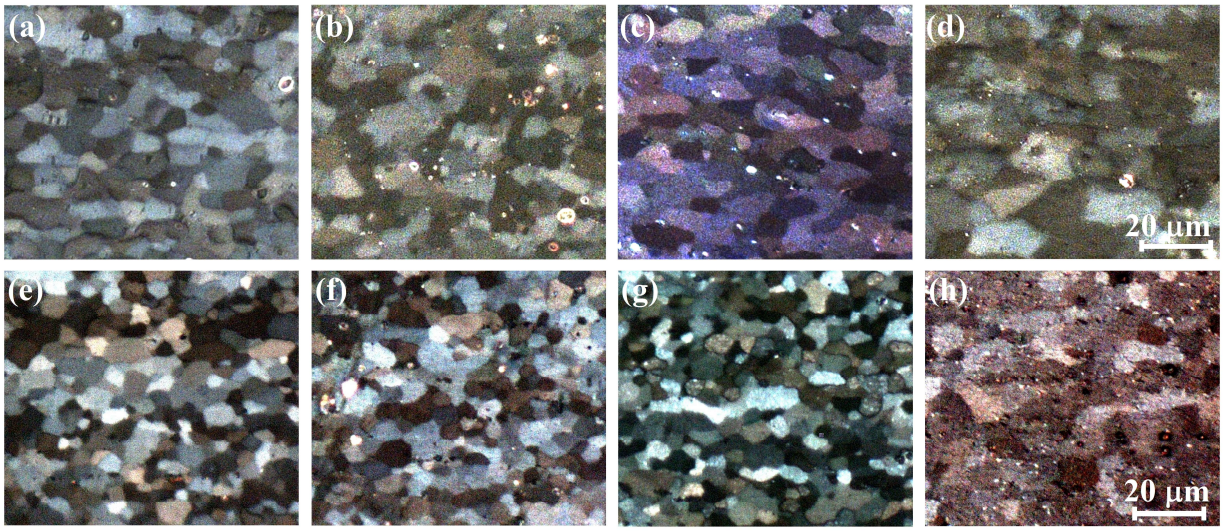

Figure 4. Microstructure after annealing at 480 °C for 15 min: (a–d) furnace annealing in air; (e–h) saltpeter (480 °C, 5 min) followed by furnace annealing in air at 480 °C for 15 min. Alloys: (a, e) AlMg; (b, f) AlMg0.4Zn; (c, g) AlMg0.7Zn; (d, h) AlMg0.7Cu.

Table 2. Mean grain size after annealing.

Alloy	Air at 480 °C (15 min), μm	Saltpeter 480 °C (5 min), μm	Saltpeter + air at 480 °C (15 min), μm
AlMg	8.5 ± 0.3	3.9 ± 0.2	4.0 ± 0.2
AlMg0.4Zn	8.5 ± 0.3	3.9 ± 0.2	4.0 ± 0.2
AlMg0.7Zn	8.7 ± 0.3	3.9 ± 0.3	3.9 ± 0.3
AlMg0.7Cu	11.5 ± 2	4.0 ± 0.3	4.5 ± 0.5

Annealing in air results in a mean grain size of 7.5–7.7 μm for the AlMg and Zn-modified alloys and 11.5 μm for the Cu-modified alloy. Rapid heating in the saltpeter bath produces finer grains, with sizes of 4.0–4.5 μm for all studied alloys. The minor variations are within the experimental scatter, suggesting that the additions of Zn and Cu do not significantly influence the recrystallized grain size obtained after saltpeter annealing.

Tensile tests at temperatures of 480–520 °C confirm the superplastic behavior of the alloys (Figure 5).

To estimate the strain rate range of superplastic behavior, tests with a step-by-step increase in a strain rate were performed. The strain rate m as a function of strain rate exhibits a typical sigmoidal shape for all studied alloys. For the reference and Zn-containing alloys, high strain rate sensitivity (above 0.5), corresponding to the liner part (part II) in a logarithmic scale, is observed in a strain rate range of 1×10^{-3} to 1×10^{-2} s^{-1} with the maximum strain rate m of 0.55–0.61 near 3×10^{-3} s^{-1}. According to the tests, alloying with Cu shifts the maximum m-value and the optimum strain rate toward lower strain rates, where m reaches slightly higher maximum values of 0.64–0.67 at a strain rate of ~1.5×10^{-3} s^{-1}. We attribute the difference in the m-value to the weaker stability of the grain structure during low-strain-rate deformation in the Cu containing alloy, which has an impact on the stress–strain rate curve and influences the m value.

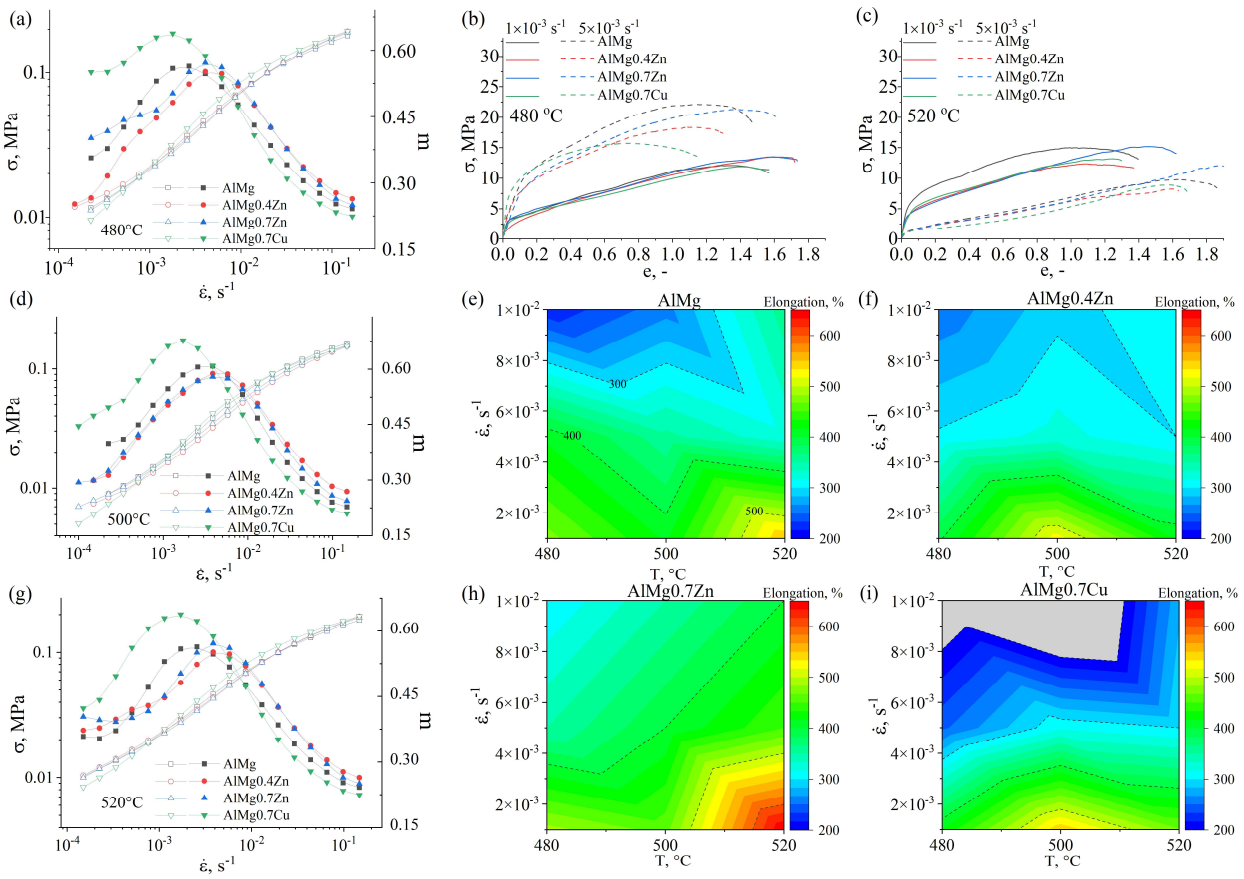

Figure 5. Tensile testing results for the AlMg, AlMg0.4Zn, AlMg0.7Zn, and AlMg0.7Cu alloys: (a, d, g) strain rate sensitivity; (b, c) true stress–strain curves at 480 and 520 °C for strain rates of 5×10^{-3} and 1×10^{-3} s^{-1}; (e, f, h, i) contour maps of elongation-to-failure as a function of temperatures 480–520 °C and strain rates 10^{-3}–10^{-2} s^{-1}.

It is notable that the addition of 0.7% Zn increases elongation values, especially at a temperature of 520 °C, providing nearly 650% elongation at strain rates of (1–2) × 10^{-3} s^{-1}. The Zn-modified alloys (AlMg0.4Zn and AlMg0.7Zn) exhibit lower flow stresses compared to the reference AlMg alloy. The AlMg0.7Cu alloy demonstrates good superplastic properties at a smaller strain rate (1–2) × 10^{-3} s^{-1} with elongation to failure of 450% to 550%, whereas the elongation decreases below 350% at 5×10^{-3} s^{-1}. To avoid significant grain growth, we chose the regime with higher strain rate 5×10^{-3} s^{-1} and lower temperature of 480 °C for a detailed analysis of the deformation mechanisms via post-deformation microstructure characterization and marker grid measurements. This regime provides the similar *m*-value and the same grain size (Figure 6) for the alloys.

After annealing, the grains remain nearly equiaxed, with only slight growth from (4.0–4.2) ± 0.3 to (4.9–5.2) ± 0.3 μm when the annealing time was extended from 20 to 35 min. The longitudinal grain size increases with strain, while the transverse size is nearly constant (4.0–4.6 μm) across the alloys (Figure 6 and 7a).

Grain growth occurs in the longitudinal direction (Figure 7a), and the grain aspect ratio (L// and L⊥) increases from ~1.1 before straining to ~1.5 after failure (Figure 7b), confirming grain elongation along the tensile direction (Figure 7c). The continuous increase in aspect ratio indicates that intragranular mechanisms contribute to superplastic deformation under the studied deformation regime.

No pronounced differences in grain size, subgrain size, or the LAGB/HAGB ratio are observed between the alloys (Figure 6a–f). Moreover, local misorientation analysis reveals a higher kernel angle misorientation (KAM) value and ~40% higher geometrically necessary dislocation (GND) density after a strain of 0.69 at 480 °C and 5 × 10^{-3} s^{-1} for the Cu-containing alloy compared to the other alloys (Figure 6g–l).

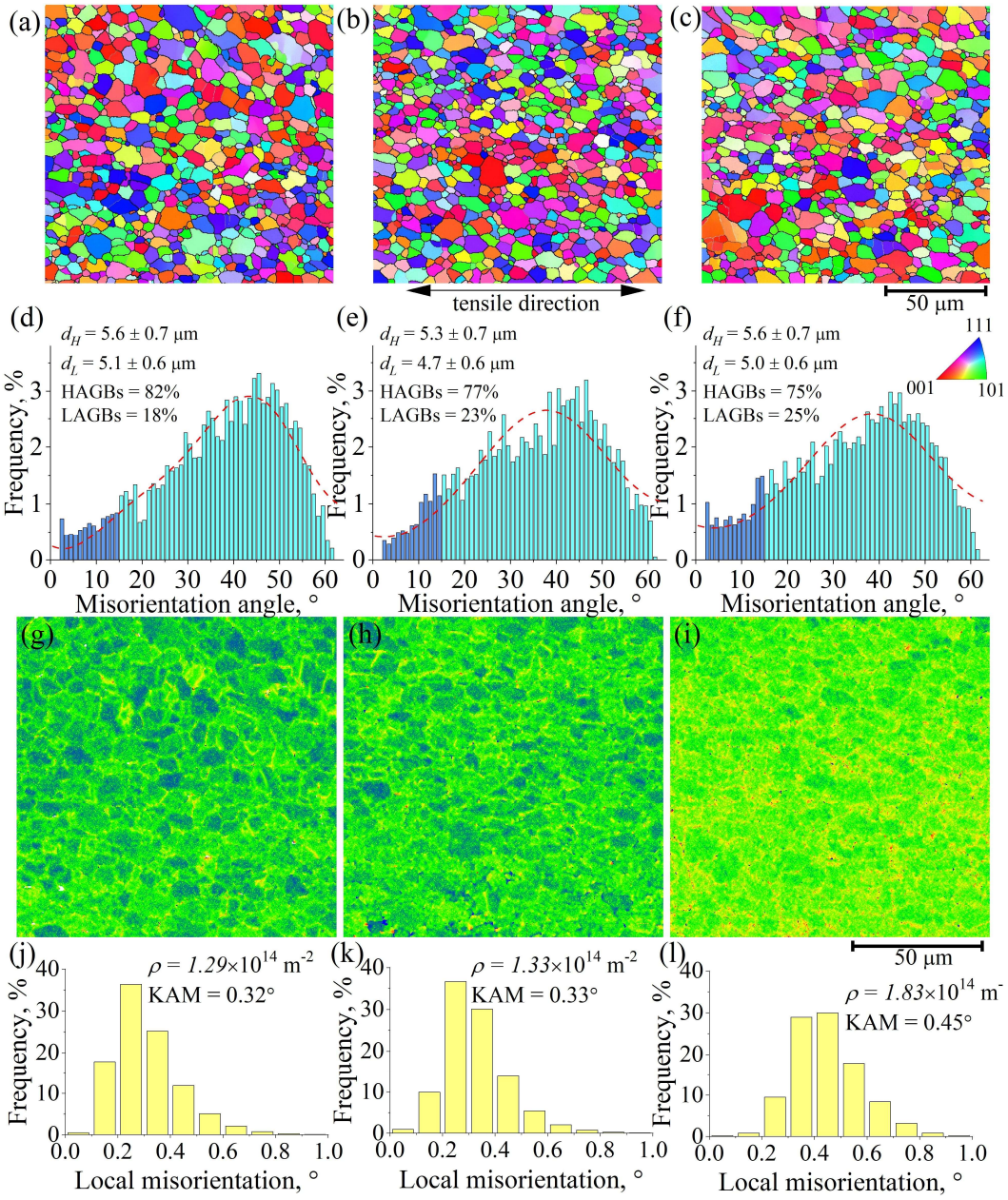

Figure 6. Electron backscatter diffraction data: (a–c) inverse pole figures contract images with (d–f) misorientation angle distributions (white colored lines are LAGBs and black colored lines are HAGBs) and (g–i) local misorientation analysis with (j–l) local misorientation angle distributions for the reference (a, d, g, j) AlMg, (b, e, h, k) AlMg0.7Zn, and (c, f, i, l) AlMg0.7Cu alloys after a strain of 0.69 at 480 °C and 5 × 10^{-3} s^{-1}; KAM is kernel misorientation angle; d_H is equivalent diameter for grains; d_L is equivalent diameter for subgrains, ρ is geometrically necessary dislocation density.

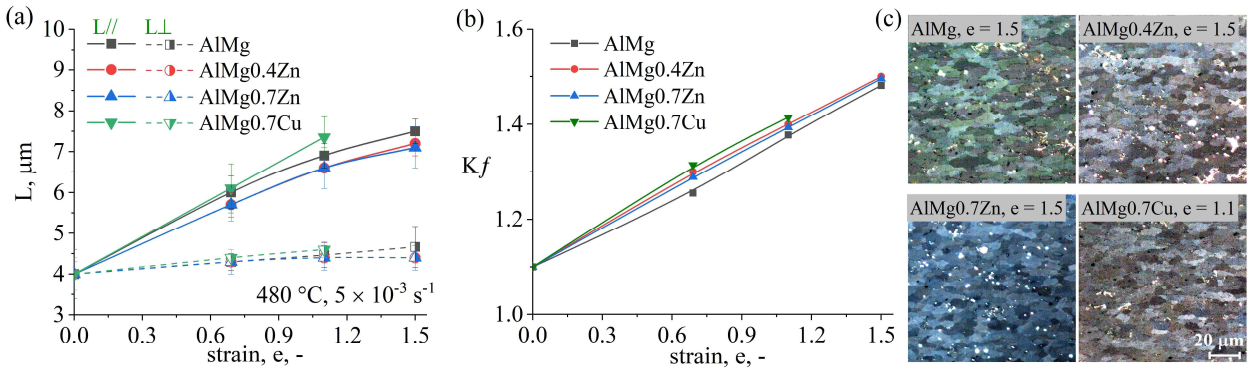

Figure 7. Evolution of (a) a mean grain size in the longitudinal (L//) and transverse (L⊥) directions and (b) grain aspect ratio (K*f*) vs strain (e is a logarithmic strain); (c) the grain structure after deformation near failure.

Before the onset of the superplastic deformation, dispersoids were uniformly distributed within grain interiors (Figure 8a–c). After deformation, the formation of precipitate-depleted zones (PDZ) and the redistribution of dispersoids are observed (Figure 8d–f). Fine dispersoids accumulate at grain boundaries along the tensile direction and coarsen (green arrow). In the AlMg0.7Cu alloy, Mn- and Cu-bearing dispersoids (T-phase, blue arrow) exhibit higher fraction of platelet-like particles, and particles coarsen significantly at the grain boundaries during superplastic deformation. No residual cavities are observed at a strain of 0.69 for all alloys studied. At a strain of 1.1, the cavity fraction is negligibly low (<0.3%) for all alloys, while it is about 1.2% for the Cu containing alloy. After failure, at the strain of above 1.5 in the Cu-free alloys, the fraction of cavities is from 1.1% to 1.5%.

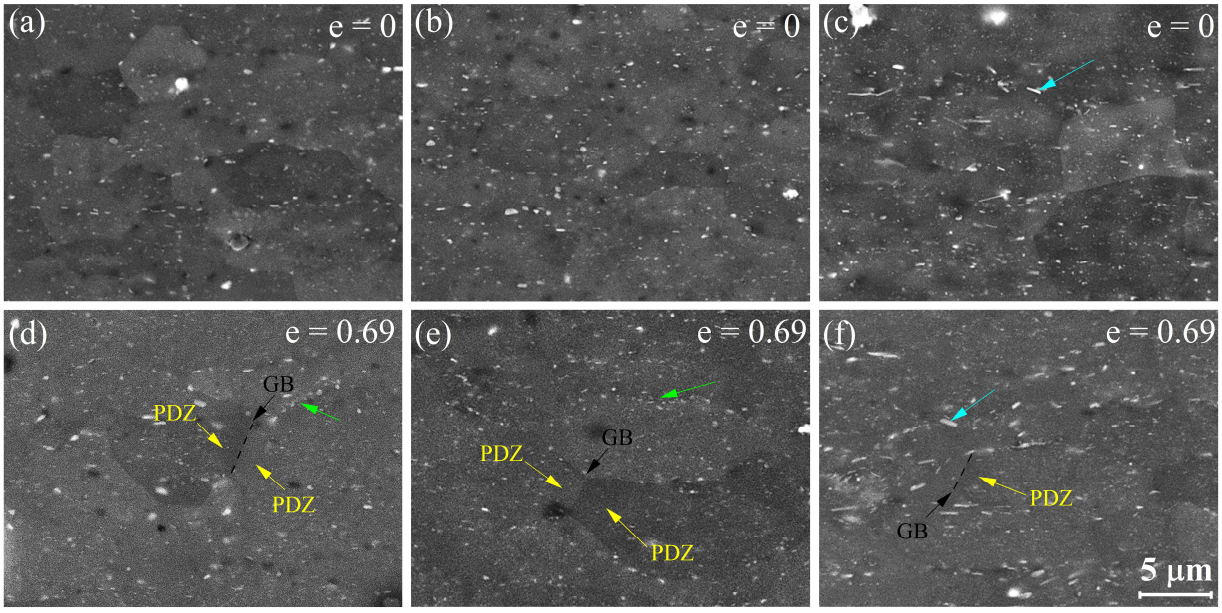

Figure 8. SEM images showing particle redistribution (a–c) before (e = 0) and (d–f) after a strain of e = 0.69 at 480 °C and 5 × 10^{-3} s^{-1} for the (a, d) AlMg, (b, e) AlMg0.7Zn, and (c, f) AlMg0.7Cu alloys; PDZ is precipitation depleted zone and GB is grain boundary.

To quantitatively assess the GBS contribution to the total strain, samples were first pre-strained to e = 0.69 at 480 °C and 5 × 10^{-3} s^{-1}. This pre-deformation corresponded to the onset of steady-state flow. The pre-polished samples with FIB grids were subjected to additional stepwise deformation (10%–15% increments) to analyze the microstructure evolution (Figure 9). The displacements of the grid lines at grain boundaries were measured after each step, and the total strain was partitioned into three components: strain accommodated by GBS (ε_{GBS}), intragranular strain (ε_{in}), and strain localized at the across grain boundaries in striation regions (ε_{str}).

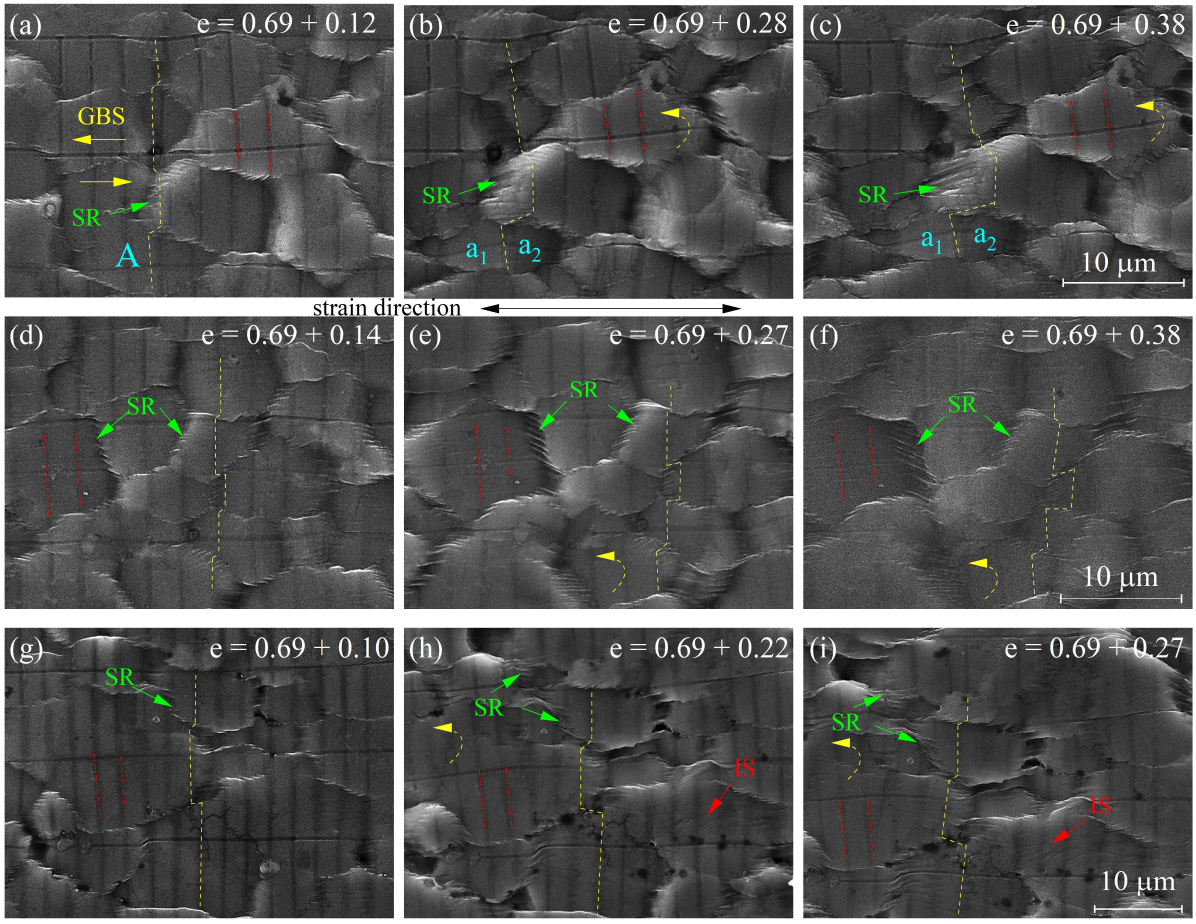

Figure 9. Surface marker grid evolution with strain (from e = 0.69 to 0.96–1.07) at 480 °C and 5 × 10^{-3} s^{-1} for (a–c) AlMg, (d–f) AlMg0.7Zn, and (g–i) AlMg0.7Cu alloys. Yellow dashed lines show grain boundary sliding (GBS) displacements; green arrows show striation regions (SR); red arrows show intragranular deformation (IS).

The AlMg reference alloy shows a GBS contribution of ~31%, an intragranular strain contribution of ~18%, and the striation regions occupation of ~50% (Table 3).

The high striation contribution suggests heterogeneous deformation, with a significant portion of strain accommodated in localized bands rather than by uniform GBS or intragranular slip. The Zn-modified alloys exhibit a higher GBS contribution (~40%) compared with the reference alloy, while the intragranular strain contribution is similar (~20%), and the strain localized in the striation regions contributes ~40%. The AlMg0.7Cu alloy shows distinctly different behaviors. The folds

develop on the surface of the grain bodies of the Cu-bearing alloy. The GBS contribution (~30%) is similar to the reference alloy, while the intragranular strain contribution is ~30%, which is significantly higher, whereas the striation contribution is lower (~40%), comparable to the Zn-modified compositions. Thus, copper addition does not affect the GBS contribution but facilitates intragranular deformation via dislocation creep, which agrees to EBSD data.

Table 3. Contributions of deformation mechanisms at 480 °C and 5×10^{-3} s^{-1}.

Alloy	Total strain (–)	GBS strain via GBS shifts	GBS contribution (%)	Intragranular strain (–)	Intragranular strain contribution (%)	Striation region strain (–)	Striations contribution (%)
AlMg	0.69 + 0.12	0.036 ± 0.005	31 ± 4	0.019 ± 0.005	16 ± 4	0.06 ± 0.005	51 ± 5
	0.69 + 0.28	0.087 ± 0.006	31 ± 2	0.05 ± 0.01	18 ± 4	0.14 ± 0.01	50 ± 5
	0.69 + 0.38	0.117 ± 0.012	31 ± 3	0.07 ± 0.01	18 ± 3	0.19 ± 0.01	51 ± 5
AlMg 0.4Zn	0.69 + 0.15	0.063 ± 0.005	42 ± 3	0.023 ± 0.006	15 ± 4	0.07 ± 0.01	45 ± 7
	0.69 + 0.31	0.123 ± 0.012	40 ± 4	0.05 ± 0.01	17 ± 4	0.14 ± 0.02	46 ± 7
	0.69 + 0.40	0.164 ± 0.012	41 ± 3	0.07 ± 0.01	17 ± 3	0.17 ± 0.02	43 ± 5
AlMg 0.7Zn	0.69 + 0.14	0.054 ± 0.004	39 ± 3	0.031 ± 0.004	22 ± 3	0.05 ± 0.01	40 ± 7
	0.69 + 0.27	0.113 ± 0.012	42 ± 4	0.05 ± 0.01	20 ± 4	0.11 ± 0.02	41 ± 7
	0.69 + 0.38	0.154 ± 0.016	41 ± 4	0.08 ± 0.01	22 ± 3	0.15 ± 0.02	40 ± 5
AlMg 0.7Cu	0.69 + 0.10	0.031 ± 0.004	31 ± 4	0.033 ± 0.004	33 ± 4	0.04 ± 0.006	36 ± 6
	0.69 + 0.22	0.067 ± 0.006	30 ± 3	0.06 ± 0.01	30 ± 4	0.09 ± 0.004	38 ± 2
	0.69 + 0.27	0.081 ± 0.008	30 ± 3	0.08 ± 0.01	30 ± 4	0.11 ± 0.008	40 ± 3

4. Discussion

The key differences between the alloys with and without Cu are in the Mn-bearing precipitate's parameters. In the reference alloy and Zn bearing alloys, the precipitates of the Al_6Mn phase [48] with dissolved Cr exhibit a near-equiaxed shape and a near-homogeneous size distribution before superplastic deformation. After superplastic deformation, some coarsening of precipitates is observed at the grain boundaries while the precipitates retain near-equiaxed shape. These dispersoids effectivity pin grain boundaries and provide a stable fine-grained structure in a wide temperature range of 480–520 °C, resulting in elongation to failure of 320%–350% at 5×10^{-3} s^{-1} and 480%–550% at 1×10^{-3} s^{-1} for the reference alloy. The addition of Zn significantly influences the grain size but effectively decreases stress values and increases the mean elongation to 350%–420% at 5×10^{-3} s^{-1} and 490%–650% at 1×10^{-3} s^{-1}.

The Cu-modified alloy exhibits a bimodal size distribution of dispersoids, consisting of fine equiaxed and platelet-like precipitates, and both types are enriched with Mn and Cu. TEM data indicate that the dominant fraction of precipitates belongs to the T($Al_{20}Cu_2Mn_3$) or similar (Al,Cu,Mn) phases [49–52]. The Cu- and Mn-bearing precipitates grow rapidly at GBs during superplastic deformation and are less effective for Zener pinning, especially at elevated temperatures. Coarsening of these precipitates at GBs leads to a weakening superplastic behavior for the Cu bearing alloy with elongations of 250%–300% at 5×10^{-3} s^{-1} and 420%–520% at 1×10^{-3} s^{-1}.

However, grain size stability is not the only factor influencing the deformation behavior. After straining to 0.69 at the relatively low temperature of 480 °C, the grain size is similar for all studied alloys (~5 μm), while the contributions of the deformation mechanisms differ between Zn and Cu-modified alloys. The grain aspect ratio increases with straining, indicating grain elongation along the tensile direction, which suggests that dislocation and diffusional creep are operated during deformation. These data agree with the behavior of the Al-Mg based 5083 alloy with a coarser grain structure at subsolidus temperatures [15,19,53].

The Al-Mg based alloys with grain sizes of 6–12 μm demonstrate a comparatively weak grain boundary sliding contribution to the total strain, which is below 25%, during subsolidus superplastic deformation at 540 ± 10 °C (0.97–0.98 $T_{i.m.}$) [15,19,31]. This value is significantly lower than that of Al-Zn-Mg based alloys, where GBS contributes 40%–60% [32,54,55]. The GBS contribution increases during the steady flow stage of superplastic deformation in Al-Mg based alloys [31,53]. At the relatively low deformation temperature studied here, the reference AlMg alloy exhibits a GBS contribution of ~30%, which is consistent with literature data. A comparison of the data for Zr-free Al-Mg-Mn-Cr alloys with the studied Zr-containing alloys suggests that nanoscale Al_3Zr precipitates do not weaken GBS. The volume fraction of PDZs, associated with diffusion mass transfer, is only 15%, which is significantly lower than at subsolidus temperatures and low strain rates [15,31,34]. The addition of 0.4–0.7 wt.% Zn increases the GBS contribution to ~40%, bringing it into the range typical of Al-Zn-Mg based alloys with higher Zn content.

The observed difference in GBS contribution between the Zn-free and Zn-modified alloys can be rationalized at the atomic scale. According to molecular dynamics simulations and first-principles calculations, Mg atoms form strong bonds with Al, creating low-mobility Al-Mg clusters that increase the threshold stress for GBS and suppress grain boundary sliding [37,41,56]. In contrast, Zn atoms exhibit weak bonds with Al and tend to segregate at grain boundaries, forming a thick solute rich layer that substantially decreases the barriers to GBS [37,41,56]. Ab initio modeling by Kuznetsov et al. [37,57] confirmed that Zn segregation decreases the activation energy for GBS, whereas Mg segregation increases it. In the case of Cu, which also increases the barriers for GBS [58], its addition to the studied Al-Mg based alloy [57] does not influence the GBS contribution.

The formation of striation regions near transverse grain boundaries was explained by Rust and Todd [20], who confirmed that striations result from newly developed surfaces formed during superplastic flow. This interpretation agrees well with that in [11]. The striated zones develop as a result of diffusional creep accommodation and GBS involving out-of-plain grain rotation. In the studied alloys, the striated areas are extensive, indicating that diffusional creep plays an important role in accommodating GBS. The minor Zn addition facilitates GBS and decreases the fraction of striation areas, which improves the superplastic performance of the Al-Mg-Mn based alloy. The improved superplasticity of the Zn-bearing alloys, achieved through enhanced GBS, increases the efficiency of superplastic forming by expanding the favorable temperature-strain rate window and by providing higher elongation to failure.

In contrast, Cu alloying facilitates coarsening of the dispersoids at the longitudinal grain boundaries and enhances intragranular deformation by promoting dislocation-controlled creep [59,60]. Higher dislocation activity is confirmed by the evolution of the surface structure and by the values of geometrically necessary dislocation density estimated after superplastic deformation. Intragranular deformation facilitates grain elongation along the rolling direction. As a result, Cu alloying weakens the superplastic behavior of the studied alloys. Lower elongations are observed even at the optimum

strain rate values of 1×10^{-3} s^{-1} despite the higher strain rate sensitivity and smaller flow stresses. This phenomenon can be attributed to the higher residual cavitation fraction in the Cu-bearing alloy, which initiates premature failure during superplastic deformation. Further experiments over a wider temperature, strain rates, and grain sizes are required to elucidate the effect of Cu on the superplastic performance of Al-Mg based alloys, to construct deformation mechanism maps, and to clarify the effects of alloying elements over broader temperature and strain rate ranges.

5. Conclusions

The effect of Zn and Cu additions on the superplasticity of the Al-5.2Mg-0.9Mn-0.12Cr-0.1Zr alloy was studied by analyzing deformation behavior and strain-induced microstructural evolution in the sample interior and on the surface (shears and rotations) via the evolution of FIB-milled grids.

The addition of Zn increases elongation to failure from 350%–550% to 450%–650% in strain rate range of (1–5) × 10^{-3} s^{-1} and in a temperature range of 480 to 520 °C, while the addition of Cu decreases elongation to 250%–300%.

Under the selected thermomechanical processing and deformation conditions (480 °C, 5×10^{-3} s^{-1}, true strain of 0.69), the mean grain size remains similar for all alloys (~5.5 μm). Therefore, the observed differences in superplastic ductility are not attributable to variations in grain size or its thermal stability, but rather to redistribution of specific deformation mechanisms. The observed improvements with Zn addition are consistent with atomic-scale predictions: Zn segregation lowers the energy barrier to GBS, whereas Mg and Cu increase it.

The addition of 0.4–0.7 wt.% Zn increases the contribution of grain boundary sliding to the total strain from ~30% to ~40% while reducing the contribution of diffusion-creep-induced striation zones. Favoring GBS is correlated with enhanced superplastic behavior. The beneficial effect of Zn is rationalized by its known tendency to segregate at grain boundaries, reducing the activation barrier for GBS.

In contrast, the addition of 0.7 wt.% Cu does not influence the GBS contribution in the high Mg content alloy, but promotes intragranular deformation, increasing its contribution from 15%–20% to about 30% of the total strain. This enhanced intragranular straining, associated with the dislocation slip/creep mechanism (evidenced by higher GND density and grains surface folding), is the primary cause of reduced superplastic performance. Furthermore, Mn and Cu-bearing dispersoids at grain boundaries coarsen more rapidly and are less effective in Zener pinning, promoting cavitation and premature failure.

The presence of fine Al_3Zr precipitates (~10–25 nm) in all alloys does not impede GBS; the reference alloy exhibits ~30% GBS, which is higher than that reported for Zr-free Al-Mg-Mn-Cr alloys under similar conditions.

The results provide a scientific basis for compositional optimization of Al-Mg-Mn-based alloys for superplastic forming. Zn is identified as a beneficial minor addition that enhances formability, whereas Cu is detrimental under most of the studied regimes and should be avoided or tightly controlled in such alloys.

Use of AI tools declaration

The authors declare they have not used Artificial Intelligence (AI) tools in the creation of this article.

Acknowledgments

Transmission electron microscopy of the precipitates and EBSD studies were supported by the Russian Science Foundation (Grant No. 23-19-00791-П). The deformation behavior and deformation mechanism analysis were investigated under the Russian Science Foundation Grant No. 23-79-01155.

Author contributions

Conceptualization: A.V.M.; methodology: Z.S.T, A.V.M. and O.A.Y.; software: E.S.S.; validation: Z.S.T., A.V.M.; formal analysis: O.A.Y. and E.S.S.; investigation: Z.S.T., O.A.Y., A.V.M., N.Y.T and V.V.C.; resources: A.V.M. and O.A.Y.; data curation: Z.S.T., N.Y.T and V.V.C.; writing—original draft preparation: Z.S.T.; writing—review and editing: A.V.M., visualization: Z.S.T. and E.S.S.; supervision: A.V.M.; project administration: A.V.M. and O.A.Y.; funding acquisition: A.V.M. and O.A.Y. All authors have read and agreed to the published version of the manuscript.

Conflict of interest

The authors declare no conflict of interest.

References

1. Heinz A, Haszler A, Keidel C, et al. (2000) Recent development in aluminium alloys for aerospace applications. *Mater Sci Eng A* 280: 102–107. https://doi.org/10.1016/S0921-5093(99)00674-7
2. Aamir M, Giasin K, Tolouei-Rad M, et al. (2020) A review: Drilling performance and hole quality of aluminium alloys for aerospace applications. *J Mater Res Technol* 9: 12484–12500. https://doi.org/10.1016/J.JMRT.2020.09.003
3. Dursun T, Soutis C (2014) Recent developments in advanced aircraft aluminium alloys. *Mater Des* 56: 862–871. https://doi.org/10.1016/J.MATDES.2013.12.002
4. Li Z, Zhan M, Fan X, et al. (2023) Effect of blank quenching on shear spinning forming precision of 2219 aluminum alloy complex thin-walled components. *Chin J Aeronaut* 36: 538–555. https://doi.org/10.1016/j.cja.2022.11.027
5. Barnes AJ (2001) Industrial applications of superplastic forming: Trends and prospects. *Mater Sci Forum* 357–359: 3–16. https://doi.org/10.4028/www.scientific.net/MSF.357-359.3
6. Aksenov S, Sorgente D (2020) Determination of biaxial stress–strain curves for superplastic materials by means of bulge forming tests at constant stress. *CIRP J Manuf Sci Technol* 31: 618–627. https://doi.org/10.1016/j.cirpj.2020.09.002
7. Zhang Z, Jia Z, Ding L, et al. (2025) Achieving equiaxial fine grains and high superplasticity of Al-Zn-Mg-Cu alloy by an improved thermo-mechanical treatment. *Mater Charact* 230: 115806. https://doi.org/10.1016/j.matchar.2025.115806
8. Zhang Z, Xiang K, Ding L, et al. (2026) Achieving grain refinement and excellent superplasticity in Al-Zn-Mg-Cu alloy by the coupling of rolling and annealing. *Mater Sci Eng A* 962: 150206. https://doi.org/10.1016/j.msea.2026.150206

9. Wang YN, Huang JC (2003) Comparison of grain boundary sliding in fine grained Mg and Al alloys during superplastic deformation. *Scr Mater* 48: 1117–1122. https://doi.org/10.1016/S1359-6462(02)00615-2
10. Lu P, Huang H, Ren Q, et al. (2024) Effect of initial grain structure on the microstructure evolution and superplastic behavior of Al-Mg-Sc-Zr alloy. *Mater Charact* 210: 113792. https://doi.org/10.1016/j.matchar.2024.113792
11. Masuda H, Sato E (2020) Diffusional and dislocation accommodation mechanisms in superplastic materials. *Acta Mater* 197: 235–252. https://doi.org/10.1016/j.actamat.2020.07.042
12. Todd RI (2000) Critical review of mechanism of superplastic deformation in fine grained metallic materials. *Mater Sci Technol* 16: 1287–1294. https://doi.org/10.1179/026708300101507118
13. Figueiredo RB, Langdon TG (2022) Effect of grain size on strength and strain rate sensitivity in metals. *J Mater Sci* 57: 5210–5229. https://doi.org/10.1007/s10853-022-06919-0
14. Kawasaki M, Langdon TG (2007) Principles of superplasticity in ultrafine-grained materials. *J Mater Sci* 42: 1782–1796. https://doi.org/10.1007/s10853-006-0954-2
15. Sotoudeh K, Bate PS (2010) Diffusion creep and superplasticity in aluminium alloys. *Acta Mater* 58: 1909–1920. https://doi.org/10.1016/j.actamat.2009.11.034
16. Lin YC, Li QF, Xia YC, et al. (2012) A phenomenological constitutive model for high temperature flow stress prediction of Al-Cu-Mg alloy. *Mater Sci Eng A* 534: 654–662. https://doi.org/10.1016/j.msea.2011.12.023
17. Zou G, Chen S, Xu Y, et al. (2024) Microstructural evolution and deformation mechanisms of superplastic aluminium alloys: A review. *Trans Nonferrous Met Soc China* 34: 3069–3092. https://doi.org/10.1016/S1003-6326(24)66596-9
18. Sharifullina ER, Shveykin AI, Trusov PV, et al. (2026) Multilevel model considering the influence of alloying additions for describing superplasticity of aluminum alloys. *Phys Mesomech* 29: 306–320. https://doi.org/10.1134/S1029959925601150
19. Mikhaylovskaya AV, Yakovtseva OA, Golovin IS, et al. (2015) Superplastic deformation mechanisms in fine-grained Al-Mg based alloys. *Mater Sci Eng A* 627: 31–41. https://doi.org/10.1016/j.msea.2014.12.099
20. Rust MA, Todd RI (2011) Surface studies of region II superplasticity of AA5083 in shear: Confirmation of diffusion creep, grain neighbour switching and absence of dislocation activity. *Acta Mater* 59: 5159–5170. https://doi.org/10.1016/j.actamat.2011.04.051
21. Rust MA, Todd RI (2007) High resolution surface studies of superplastic deformation. *Mat Sci Forum* 551–552: 615–620. https://doi.org/10.4028/www.scientific.net/MSF.551-552.615
22. Edalati K, Ahmed AQ, Akrami S, et al. (2024) Severe plastic deformation for producing superfunctional ultrafine-grained and heterostructured materials: An interdisciplinary review. *J Alloys Compd* 1002: 174667. https://doi.org/10.1016/j.jallcom.2024.174667
23. Mao X, Yi Y, Huang S, et al. (2021) Grain refinement and thermal stability of 2219 aluminum alloy in the warm deformation process. *Met Mater Int* 27: 4564–4576. https://doi.org/10.1007/s12540-020-00898-0
24. Liu L, Wu Y, Gong H, et al. (2018) A physically based constitutive model and continuous dynamic recrystallization behavior analysis of 2219 aluminum alloy during hot deformation process. *Materials* 11: 1443. https://doi.org/10.3390/ma11081443

25. Xiao H, Li Y, Geng J, et al. (2021) Effects of nano-sized TiB_2 particles and Al_3Zr dispersoids on microstructure and mechanical properties of Al-Zn-Mg-Cu based materials. *Trans Nonferrous Met Soc China* 31: 2189–2207. https://doi.org/10.1016/S1003-6326(21)65648-0
26. Li Y, Lu B, Yu W, et al. (2021) Two-stage homogenization of Al-Zn-Mg-Cu-Zr alloy processed by twin-roll casting to improve $L1_2$ Al_3Zr precipitation, recrystallization resistance, and performance. *J Alloys Compd* 882: 160789. https://doi.org/10.1016/j.jallcom.2021.160789
27. Duan T, Li J, Zou G, et al. (2026) Microstructural evolution and deformation mechanisms during superplastic deformation of a banded-grained high entropy alloy. *Mater Charact* 237: 116523. https://doi.org/10.1016/j.matchar.2026.116523
28. Humphrey FJ, Hatherly M (2004) *Recrystallization and Related Annealing Phenomena*, Pergamon: Elsevier. https://doi.org/10.1016/B978-0-08-044164-1.X5000-2
29. Sidor JJ, Petrov RH, Kestens LAI (2011) Modeling the crystallographic texture changes in aluminum alloys during recrystallization. *Acta Mater* 59: 5735–5748. https://doi.org/10.1016/j.actamat.2011.05.050
30. Hu Z, Qian F, Li J, et al. (2026) Modulated precipitation of dispersoids and strength-ductility synergy via multi-step pre-treatments in an Al-Mg-Mn-Fe-Zr-Cr-Si alloy. *Mater Sci Eng A* 953: 149809. https://doi.org/10.1016/j.msea.2026.149809
31. Mikhaylovskaya AV, Yakovtseva OA, Irzhak AV (2022) The role of grain boundary sliding and intragranular deformation mechanisms for a steady stage of superplastic flow for Al-Mg-based alloys. *Mater Sci Eng A* 833: 142524. https://doi.org/10.1016/j.msea.2021.142524
32. Mikhaylovskaya AV, Yakovtseva OA, Sitkina MN, et al. (2018) Comparison between superplastic deformation mechanisms at primary and steady stages of the fine grain AA7475 aluminium alloy. *Mater Sci Eng A* 718: 277–286. https://doi.org/10.1016/j.msea.2018.01.102
33. Mikhaylovskaya A, Yakovtseva O, Sitkina M, et al. (2020) Grain-boundary and intragranular deformation in ultrafine-grained aluminum-based alloy at high strain rate. *Mater Lett* 276: 128242. https://doi.org/10.1016/j.matlet.2020.128242
34. Mikhaylovskaya AV, Yakovtseva OA, Mochugovskiy AG, et al. (2022) Influence of minor Zn additions on grain boundary anelasticity, grain boundary sliding, and superplasticity of Al-Mg-based alloys. *J Alloys Compd* 926: 166785. https://doi.org/10.1016/j.jallcom.2022.166785
35. Luo L, Liu Z, Bai S, et al. (2020) Hot deformation behavior considering strain effects and recrystallization mechanism of an Al-Zn-Mg-Cu alloy. *Materials* 13: 1743. https://doi.org/10.3390/ma13071743
36. Straumal BB, Gornakova AS, Khorosheva MA, et al. (2025) The influence of grain boundary wetting on the mechanical properties of AMg6 polycrystals. *J Surf Investig* 19: 1536–1542. https://doi.org/10.1134/S1027451025702155
37. Kuznetsov A, Karkina L, Gornostyrev Y, et al. (2021) Effects of Zn and Mg segregations on the grain boundary sliding and cohesion in Al: Ab initio modeling. *Metals* 11: 631. https://doi.org/10.3390/met11040631
38. Zhao D, Lovvik OM, Marthinsen K, et al. (2018) Segregation of Mg, Cu and their effects on the strength of Al Σ5 (210) [001] symmetrical tilt grain boundary. *Acta Mater* 145: 235–246. https://doi.org/10.1016/j.actamat.2017.12.023
39. Cui Y, Song K, Bao Y, et al. (2023) Effect of Cu and Mg co-segregation on the strength of the Al grain boundaries: A molecular dynamics simulation. *Comput Mater Sci* 229: 112391. https://doi.org/10.1016/j.commatsci.2023.112391

40. Kar'kina LE, Kar'kin IN, Gornostyrev YuN (2020) Effect of alloying element segregations on the grain boundary sliding in Al-Mg and Al-Ni alloy bicrystals: Atomistic modeling. *Phys Met Metallogr* 121: 817–822. https://doi.org/10.1134/S0031918X20090070
41. Du N, Qi Y, Krajewski PE, et al. (2011) The effect of solute atoms on aluminum grain boundary sliding at elevated temperature. *Metall Mater Trans A* 42: 651–659. https://doi.org/10.1007/s11661-010-0326-z
42. Levchenko VS, Portnoy VK, Novikov II (1991) Unusual low grain boundary sliding in aluminium alloy with classical features of micrograin superplasticity. Superplasticity in Advanced Materials (ICSAM-91), 39–44.
43. Watanabe H, Ohori K, Takeuchi Y (1987) Superplastic behavior of Al-Mg-Cu alloys. *Trans Iron Steel Inst Jpn* 27: 730–733. https://doi.org/10.2355/isijinternational1966.27.730
44. Novikov I (2000) Dynamic recrystallization at superplastic deformation of duralumin with initial recrystallized structure. *Scr Mater* 42: 899–904. https://doi.org/10.1016/S1359-6462(00)00310-9
45. Wang H, Zhang Z, Liu W, et al. (2025) Enhancing long-term corrosion resistance of Zn modified high-Mg aluminum alloys through optimized stabilization treatment. *J Mater Res Technol* 37: 2475–2484. https://doi.org/10.1016/j.jmrt.2025.06.179
46. Chen S, Zou G, Xu Y, et al. (2025) Effect of rolling schedule on grain refinement and superplasticity of 7475 Al-Zn-Mg-Cu alloy sheet. *J Mater Res Technol* 39: 9465–9476. https://doi.org/10.1016/j.jmrt.2025.11.192
47. Portnoy VK, Novikov II (1998) Evaluation of grain boundary sliding contribution to the total strain during superplastic deformation. *Scr Mater* 40: 39–43. https://doi.org/10.1016/S1359-6462(98)00394-7
48. Yang P, Engler O, Klaar HJ (1999) Orientation relationship between Al_6Mn precipitates and the Al matrix during continuous recrystallization in Al-1.3%Mn. *J Appl Crystallogr* 32: 1105–1118. https://doi.org/10.1107/S0021889899010870
49. Zolotorevsky VS, Belov NA, Glazoff MV (2007) Chapter five—Industrial casting aluminum alloys, In: Zolotorevsky VS, Belov NA, Glazoff MV, *Casting Aluminum Alloys*, Amsterdam: Elsevier, 327–396. https://doi.org/10.1016/B978-008045370-5.50007-9
50. Zupanič F, Dominguez PMP, Lu Y, et al. (2026) Microstructural evolution in the stir zone of a friction-stir-processed microalloyed Al-Mn-Cu alloy. *Metals* 16: 358. https://doi.org/10.3390/met16030358
51. Wang J, Dong S, Wang F, et al. (2026) Microalloying to refine intragranular precipitates and introduce thermally stable phases for significantly enhancing mechanical properties of the cast heat-resistant Al-Cu-Ce-Mn-Sc-Zr alloy. *Mater Sci Eng A* 949: 149440. https://doi.org/10.1016/j.msea.2025.149440
52. Zhou Y, Huang G, Pan S, et al. (2026) Revisiting the homogenization process in 2024 Al alloy: Role of temperatures on phase transformation and mechanical performance. *J Mater Sci Technol* 240: 129–143. https://doi.org/10.1016/j.jmst.2025.02.069
53. Hsiao IC, Huang JC (2002) Deformation mechanisms during low-and high-temperature superplasticity in 5083 Al-Mg alloy. *Metall Mater Trans A* 33: 1373–1384. https://doi.org/10.1007/s11661-002-0062-0
54. Yakovtseva OA, Sitkina MN, Kotov AD, et al. (2020) Experimental study of the superplastic deformation mechanisms of high-strength aluminum-based alloy. *Mater Sci Eng A* 788: 139639. https://doi.org/10.1016/j.msea.2020.139639

55. Masuda H, Tobe H, Hara T, et al. (2019) Three-dimensional characterization of superplastic grain boundary sliding inside Al-Zn-Mg-Cu alloy sheet. *Scr Mater* 164: 82–85. https://doi.org/10.1016/j.scriptamat.2019.01.043
56. Fujita T, Horita Z, Langdon TG (2004) Using grain boundary engineering to evaluate the diffusion characteristics in ultrafine-grained Al-Mg and Al-Zn alloys. *Mater Sci Eng A* 371: 241–250. https://doi.org/10.1016/j.msea.2003.12.042
57. Karkina L, Karkin I, Kuznetsov A, et al. (2019) Alloying element segregation and grain boundary reconstruction, atomistic modeling. *Metals* 9: 1319. https://doi.org/10.3390/met9121319
58. Zhou W, Huo Q, Wang C, et al. (2022) Effects of texture component, dislocation evolution and precipitation on the creep resistance of T5-treated Al-Mg-Si alloy with different Cu contents. *Mater Charact* 189: 111981. https://doi.org/10.1016/j.matchar.2022.111981
59. Kulas MA, Green WP, Taleff EM, et al. (2006) Failure mechanisms in superplastic AA5083 materials. *Metall Mater Trans A* 37: 645–655. https://doi.org/10.1007/s11661-006-0036-8
60. Liu X, Ye L, Tang J, et al. (2021) Superplastic deformation mechanism of an Al-Mg-Li alloy by high resolution surface studies. *Mater Lett* 301: 130251. https://doi.org/10.1016/j.matlet.2021.130251



AIMS Press

© 2026 the Author(s), licensee AIMS Press. This is an open access article distributed under the terms of the Creative Commons Attribution License (http://creativecommons.org/licenses/by/4.0)